ADVANCED FUNCTIONAL MATERIALS
www.afm-journal.de

Manipulating the Electronic Structure of Li-Rich Manganese-Based Oxide Using Polyanions: Towards Better Electrochemical Performance

Biao Li, Huijun Yan, Jin Ma, Pingrong Yu, Dingguo Xia, Weifeng Huang, Wangsheng Chu,* and Ziyu Wu**

Lithium-rich manganese-based layered oxides show great potential as high-capacity cathode materials for lithium ion batteries, but usually exhibit a poor cycle life, gradual voltage drop during cycling, and low thermal stability in the highly delithiated state. Herein, a strategy to promote the electrochemical performance of this material by manipulating the electronic structure through incorporation of boracic polyanions is developed. As-prepared $Li[Li_{0.2}Ni_{0.13}Co_{0.13}Mn_{0.54}](BO_4)_{0.015}(BO_3)_{0.005}O_{1.925}$ shows a decreased M-O covalency and a lowered O 2p band top compared with pristine $Li[Li_{0.2}Ni_{0.13}Co_{0.13}Mn_{0.54}]O_2$. As a result, the modified cathode exhibits a superior reversible capacity of 300 mA h g^{-1} after 80 cycles, excellent cycling stability with a capacity retention of 89% within 300 cycles, higher thermal stability, and enhanced redox couple potentials. The improvements are correlated to the enhanced oxygen stability that originates from the tuned electronic structure. This facile strategy may further be extended to other high capacity electrode systems.

1. Introduction

Owing to the rapid development of portable electronics, electric vehicles, and energy storage devices, the demand for lithium-ion batteries (LIBs) with a high-energy-density and long cycle life has spurred enormous research efforts to develop novel electrode materials with high performance.[1,2] Conventional layered transition metal oxide cathode materials, such as $LiCoO_2$, $LiNi_{1/3}Co_{1/3}Mn_{1/3}O_2$, and $LiNi_{0.8}Co_{0.2}O_2$, despite of their high theoretical capacities, have the disadvantage of oxygen evolution in the high delithiated state, which could cause severe thermal runaway of the cell for practical applications and lead to a low practical capacity.[3–5] Lithium rich manganese-based layered materials, $xLi_2MnO_3\bullet(1-x)Li[Ni_{1/3}Co_{1/3}Mn_{1/3}]O_2$, can deliver an anomalously high discharge capacity of more than 250 mA h g^{-1} through the activation of Li_2MnO_3 and have attracted increasing attention as promising high-capacity cathodes.[6,7] However, several drawbacks including poor cycle life, low thermal stability, and a gradual voltage drop during cycling hindered its commercial application in Li-ion batteries.[8,9] To overcome these problems, tremendous efforts have been made to realize improvement. Modification by doping using other metal elements is effective to obtain good cyclability.[10] However, doping usually causes a lowering of the capacity owing to the incorporation of inactive elements. The coating approach can also improve the rate capability and cycle stability for Li-rich layered oxides.[11,12] However, a highly continuous coating on the surface of particles is very difficult to obtain during the practical process.

Herein, we present for the first time a strategy for modulating the electronic structure by the local incorporation of polyanions to realize the improvement of the electrochemical performance of $xLi_2MnO_3\bullet(1-x)Li[Ni_{1/3}Co_{1/3}Mn_{1/3}]O_2$. The well-studied cathode material $0.5Li_2MnO_3\bullet0.5Li[Ni_{1/3}Co_{1/3}Mn_{1/3}]O_2$, which can also be written as $Li[Li_{0.2}Ni_{0.13}Co_{0.13}Mn_{0.54}]O_2$, was chosen as the target material to be modified because it can deliver a high capacity exceeding 300 mA h g^{-1} but shows a poor stability.[13,14] Polyanion-type compounds are a class of materials in which tetrahedral polyanion structure units $(XO_4)^{n-}$ and their derivatives $(X_mO_{3m+1})^{n-}$ (X = B, P, Si, S, As, Mo, or W) with strong covalent bonding combine with MO_x (M = transition metal) polyhedrals.[3] Their higher cyclability and thermal stability than conventional layered oxides, which is considered to be due to the high stability of oxygen ions, attract extensive attention, despite of their lower capacity.[15] Therefore, the merits of polyanions to stabilize the oxygen close-packed structure inspired us to use nonmetal elements, such as B, P, Si, S et al., to tune the electronic structure of the layered oxide. In this work, we show that through incorporation of the polyanions $(BO_3)^{3-}$ and $(BO_4)^{5-}$ in the Li-rich manganese-based layered material, the covalence of M-O decreases, and the top of the O 2p band is lowered as suggested by the first principle

Dr. B. Li, Dr. H. Yan, Dr. J. Ma,
Prof. Dr. P. Yu, Prof. D. Xia
Key lab of theory and technology
for advanced batteries materials
College of Engineering
Peking University
Beijing 100871, P.R. China
E-mail: dgxia@pku.edu.cn
Dr. W. Huang, Prof. W. Chu, Prof. Z. Wu
National Synchrotron Radiation Laboratory
University of Science and Technology of China
Hefei 230029, P.R. China
E-mail: chuws@ustc.edu.cn; wuzy@ustc.edu.cn

DOI: 10.1002/adfm.201400436

calculations, resulting in more stable oxygen ions under high voltage. The power of this approach is demonstrated by the facile synthesis of the Li-rich manganese-based oxide cathode material incorporated with boron polyanions, which shows a strongly improved specific capacity, cycling performance, redox potentials, and thermal stability in comparison with the pristine Li-rich cathode material.

2. Results and Discussion

$Li[Li_{0.2}Ni_{0.13}Co_{0.13}Mn_{0.54}](BO_4)_{0.75x}(BO_3)_{0.25x}O_{2-3.75x}$ (B*x*-LRM, x = 0, 0.02, 0.04, and 0.08) were successfully synthesized via a conventional solid-state reaction at 850 °C (see sample preparation in Experimental Section). Figure S1 (Supporting Information) shows typical scanning electron microscopy (SEM) and transmission electron microscopy (TEM) images of the B*x*-LRM particles, which clearly indicate that the size of the particles with smooth surface increases from about 100 nm to 400 nm for x = 0, 0.02, 0.04, and 0.08. **Figure 1**a shows the X-ray diffraction (XRD) patterns of the pristine and boracic polyanions-incorporated samples. All the peaks can be attributed to the layered α-$NaFeO_2$ structure of the R $\overline{3}$ m space group with weak superlattice reflection peaks appearing in the 2θ range of 21–35°.[16] No impurity peaks corresponding to the boron-related compounds were observed in the XRD patterns. With increasing amounts of the incorporated polyanions, both the superstructure-related peaks and the main reflections corresponding to the layered structure become more and more intense, implying that a more perfect layered structure and more ordering of Li-M-M in the transition metal layer were obtained. However, we did not find any prominent change of the lattice parameters even at high boron content from the usual XRD patterns. This could be explained by the small radius of the boron atom (0.27 Å) and its low scattering power due to its low atomic number, which will cause little change to the XRD pattern. Because X-ray absorption spectroscopy (XAS) is sensitive to the local structural variation, it can provide more information of local structure changes.

B K-edge X-ray Absorption Near Edge Structure (XANES) was employed to identify the entries of trigonal and tetrahedral coordinated B species with oxygen in the as-prepared sample, as shown in Figure 1b. For comparison, B XAS spectra of the standard samples H_3BO_3 and $Na_2B_4O_7$ were also measured. According to Fleet's work,[17–19] the boron K-edge XANES spectra are characterized by three prominent features: a sharp peak A at ≈194 eV corresponds to trigonal B (^{III}B), a broader peak B at 197–199 eV corresponds to tetrahedral B (^{IV}B), and a broad peak C is related to ^{IV}B at 200–202 eV and ^{III}B at 203–204 eV. Figure 1b shows that $Na_2B_4O_7$ consists of both trigonal BO_3 and tetrahedral BO_4 groups, while H_3BO_3 with two significant features, A and C, comprises only BO_3 groups, which agrees well with a previous report.[19] Based on the analysis above, B*x*-LRM contains both trigonal BO_3 and tetrahedral BO_4 groups. From the fitted dotted lines of the different peaks (shown in Figure 1b), we quantified the ratio ^{IV}B/^{III}B to be about 3 (3.05: 1) in B*x*-LRM according to the peak area, because the ratio of ^{IV}B/^{III}B is 1:1 in $Na_2B_4O_7$.[19] Hence, B*x*-LRM can be determined as $Li[Li_{0.2}Ni_{0.13}Co_{0.13}Mn_{0.54}](BO_4)_{0.75x}(BO_3)_{0.25x}O_{2-3.75x}$.

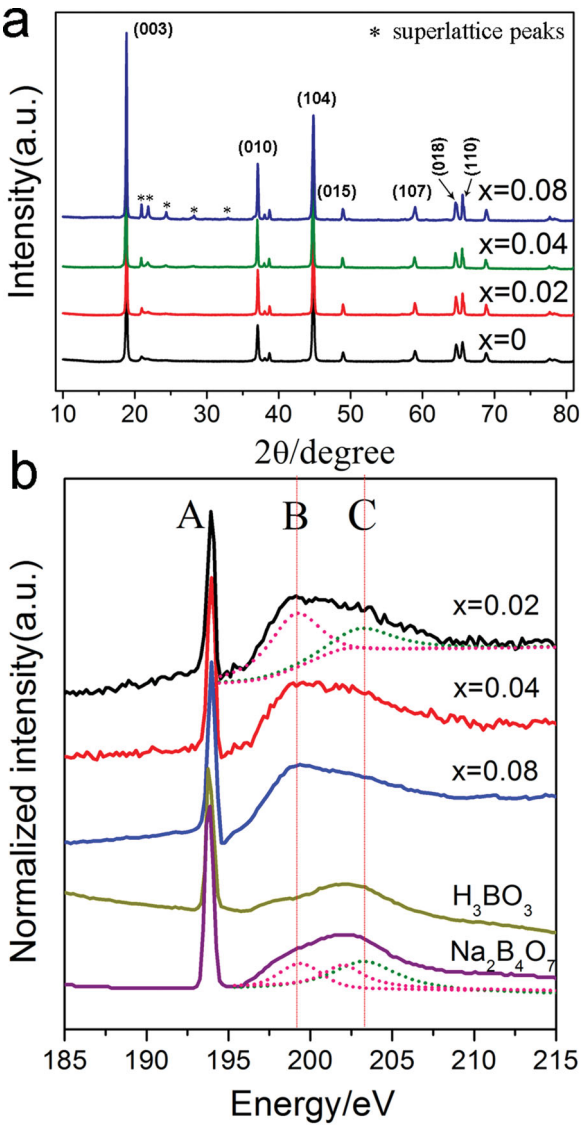

Figure 1. XRD patterns and XAS spectra of B*x*-LRM. a) XRD patterns and b) B K-edge XAS of B*x*-LRM for x = 0, 0.02, 0.04, and 0.08, and the standard samples H_3BO_3 and $Na_2B_4O_7$. The fitted pink and green dotted lines correspond to BO_4 groups and BO_3 groups, respectively.

To further investigate the local structure around the polyanion, we performed DFT simulations with a supercell of $Li_{45}[Li_9Ni_6Co_6Mn_{24}]O_{90}$ (the model is shown in the first principle calculation part 1 in the Supporting Information). We optimized four different boron tetrahedral sites in total and found that three of them remained as ^{IV}B while the other one relaxed to ^{III}B, as shown in detail in the calculation part 2 of the Supporting Information. Note that the 3:1 proportion is consistent with the ratio quantified by the boron XANES spectra. **Figure 2**a,c show the optimized crystal structure of B*x*-LRM, in which boron atoms occupy the tetrahedral interstitial sites and trigonal sites, respectively. The simulated local structure around the boracic polyanion, as shown in Figure 2b,d, shows that the M-O bonds are lengthened due to the strong B-O bond, inducing the local octahedron geometrical distortion. The

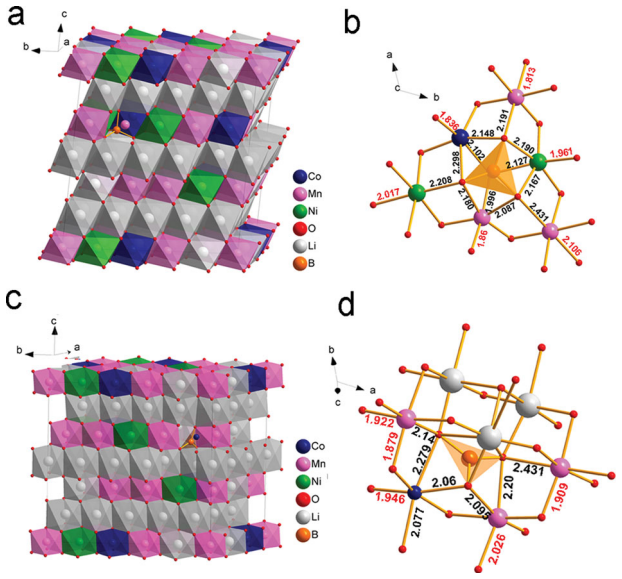

Figure 2. DFT simulated structure of B*x*-LRM. Schematic diagram of the optimized crystal structure of B*x*-LRM with a) BO4 and c) BO3; b) and d) show their local structure around the polyanion, respectively. The labeled bond lengths indicate that the M-O bonds close to boron are stretched (black number), while the bonds away from the boron atoms show a smaller length (red number). The large difference of the black and red length suggests a large distortion of the local structure.

variation of the electronic structure caused by the simultaneous structure distortion will be discussed later.

X-ray absorption fine structure (XAFS) of K-edge of Mn, Ni, and Co was measured to further reveal the local environment changes of transition metals after the boracic polyanion's incorporation. Figure S5a (Supporting Information) shows that the adsorption edge shifts to lower energy when x increases for the Mn K-edge XANES spectrum, suggesting that the boracic polyanion incorporation causes the valence of Mn to decrease in order to rebuild the charge balance of the system. Moreover, the decreased intensity of the white line peak indicates a large variation of the MnO_6 octahedral environment.[20] In addition, the pre-edge peak also exhibits an increase of intensity as a function of x, as clearly shown in the inset of Figure S5a (Supporting Information). The pre-edge peak corresponds to the electronic transition from 1s core levels to the 4p components of 3d-4p hybridized states when the MnO_6 octahedral distortion occurs, and the more distorted the octahedron is, the stronger the peak intensity of the pre-edge is.[21,22] Therefore, the increased intensity of the pre-edge peak for a high x value indicates a more distorted MnO_6 octahedron due to the boron's strong binding force with oxygen. The Fourier transformed radial structure functions of Mn K-edge XAFS (Figure S5b, Supporting Information) and the FTIR absorption spectra (Figure S5c, Supporting Information) also confirm the intensive local disorder of the MnO_6 structure and the presence of a distorted MO_6 octahedron, respectively, after the incorporation of boron. However, different from the case of Mn, the K-edge XAFS spectra of Ni and Co (Figure S6, Supporting Information) display little change, which may be due to their lower concentrations compared to Mn and the consequent lower probability to be affected by boron.

Electrochemical measurements on the Li-ion cells were performed by a galvanostatic charge-discharge technique. **Figure 3**a compares the cyclability of B0-LRM and B0.02-LRM (x = 0.02) under a 0.1 C (20 mA g^{-1}) current density in the voltage range of 2.0–4.8 V. The former shows a poor cycling performance with only 70% capacity retention, delivering 298 mA h g^{-1} at the first cycle and only 210 mA h g^{-1} at the 80th cycle. The polyanion modified material exhibits a superior cycling performance of 94% capacity retention, with 319 mA h g^{-1} at the first cycle and about 300 mA h g^{-1} at the 80th cycle. With increasing x, the capacity is reduced to 250 mA h g^{-1} for x = 0.04 and 200 mA h g^{-1} for x = 0.08 at the first cycle, but recovers to about 250 mA h g^{-1} at the 80th cycle (Figure S7a, Supporting Information). The lower capacity of the initial cycles for x = 0.08 may be attributed to the insufficient activation of the Li_2MnO_3 component for a larger particle size. But during the subsequent cycles, the activation process goes on and the capacity increases concurrently. This is consistent with Liu's work.[23] Figure 3b further compares the long cycling performance of B0-LRM and B0.02-LRM within 300 cycles (that of B0.04-LRM and B0.08-LRM are shown in Figure S7b, Supporting Information). B0-LRM shows a large capacity fading especially after 200 cycles, while for B0.02-LRM, a capacity retention of about 89% was obtained, with a reversible capacity of 200 mA h g^{-1} within 300 cycles under a 0.3 C current density of 60 mA g^{-1}. However, the rate performance of B0.02-LRM is not much improved since the size of the particles grew larger than that of B0-LRM, see Figure S7c and S7d, Supporting Information.

Moreover, the voltage degradation of B*x*-LRM is also largely buffered, as can be seen from the comparison of Figure 3c,d. After 300 cycles under a current density of 60 mA g^{-1}, B0.02-LRM still retains an average discharge voltage of 2.7 V, whereas B0-LRM shows a drastic linear voltage decline. Figure 3e plots the dQ/dV profiles of the 5th cycle for B*x*-LRM. It can be found that the redox couple potentials are enhanced substantially after the incorporation of boron. When comparing B0-LRM and B0.02-LRM, the redox couples of Mn^{4+}/Mn^{3+} and $Ni^{4+}/Ni^{3+}/Ni^{2+}$ increase from 3.02 and 3.61 to 3.44 and 3.76 V for the discharge process, respectively, and Co^{4+}/Co^{3+} also shows a slight enhancement. This leads to a higher energy density of B0.02-LRM as compared to B0-LRM.

Differential scanning calorimetry (DSC) measurements were performed to reveal the material's thermal stability, which is one of the indicators that determine the safety characteristics of the battery at elevated temperatures. Figure 3f shows that the electrodes of B0.02-LRM, charged at 4.6 V, possess a higher exothermic reaction temperature than B0-LRM, presenting intrinsically safe characteristics after the incorporation of boracic polyanions. Furthermore, we also tested the cells at 65 °C to investigate the cycling performance, and the results show that the sample B0.02-LRM has a higher stability than B0-LRM, see Figure S7e, Supporting Information.

The much improved electrochemical performance of B0.02-LRM in comparison with B0-LRM could be attributed to the electronic structural changes resulting from the proposed structural design. **Figure 4** shows the soft XAS spectra of Ni, Co, Mn, and O of B*x*-LRM, respectively. It can be found that the L_{II} and L_{III} edges of Mn, Co, and Ni for B*x*-LRM show an evident shift to lower energy as x increases, as shown in Figure 4a,b,c. L_{II} and L_{III} could be assigned to the transition of 2p3/2 and 2p1/2 core levels to an unoccupied 3d hole.[24] The shift to lower energy indicates

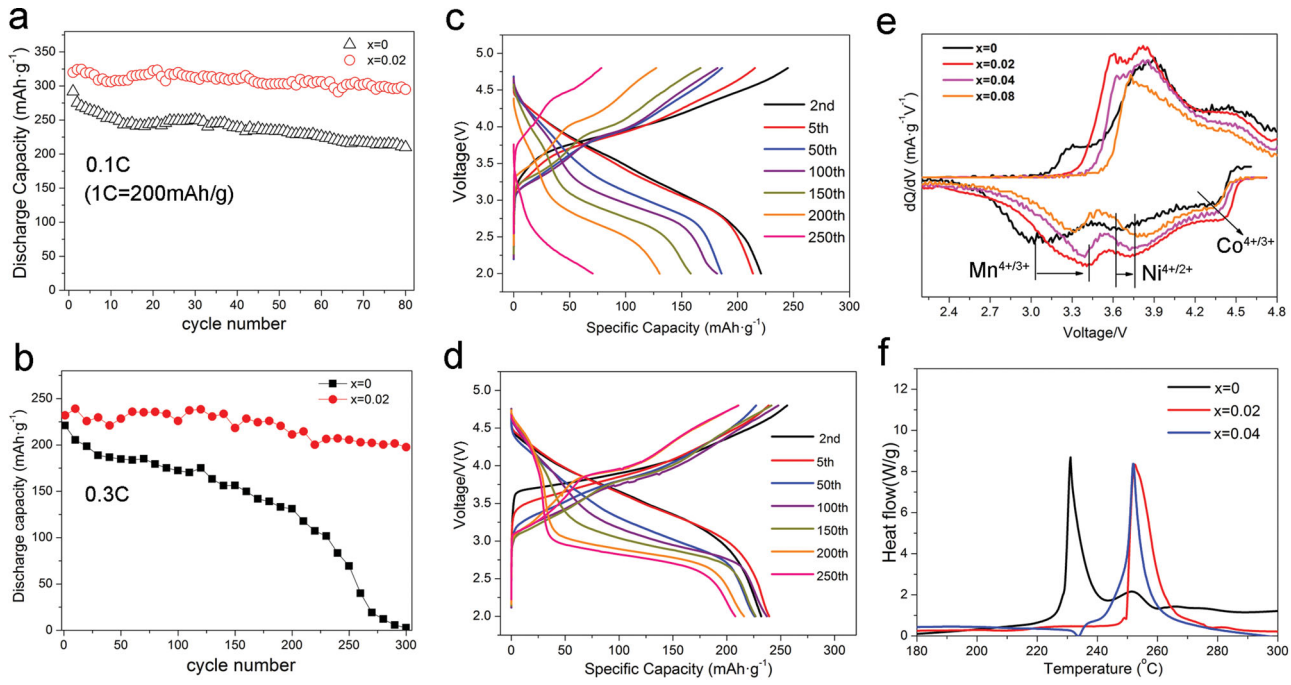

Figure 3. Electrochemical performance of B*x*-LRM. Cycling performance of B*x*-LRM with $x = 0$ and 0.02 at a current density of a) 20 mA g^{-1}, and b) 60 mA g^{-1}; Voltage evolution of B*x*-LRM with c) $x = 0$ and d) $x = 0.02$ at a current density of 60 mA g^{-1}; e) dQ/dV profiles of the 5th cycle of B*x*-LRM at a current density of 60 mA g^{-1}; f) DSC profiles of B*x*-LRM charged at 4.6 V at the second cycle and kept for 10 h at constant voltage, at a scanning rate of 10 °C/min. All of the cells are tested at room temperature.

a decrease of the valence of the transition metal and a decrease of the covalence of M-O. This electronic structural change corresponds to the local geometrical variation well shown before as the M-O bonds are lengthened due to the presence of boron. Figure 4d shows the K-edge spectra of O in these materials. The first intense peak at around 530 eV corresponds to the transition

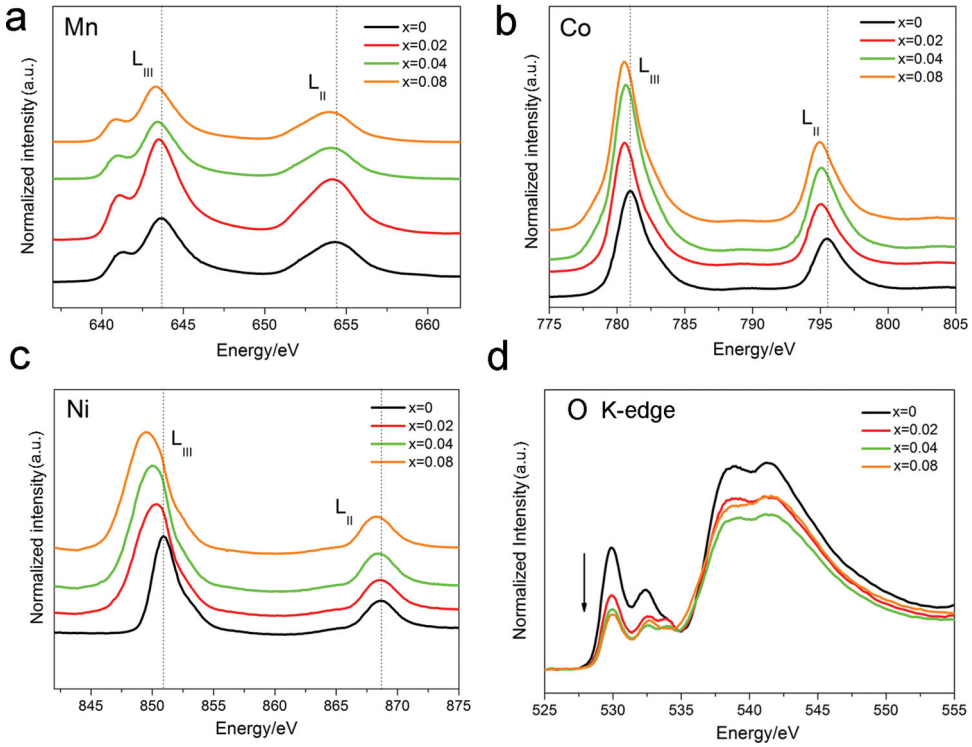

Figure 4. Electronic structural variations of B*x*-LRM. L-edge XANES spectra of a) Mn, b) Co, and c) Ni; d) O K-edge spectra of B*x*-LRM, $x = 0$, 0.02, 0.04, and 0.08.

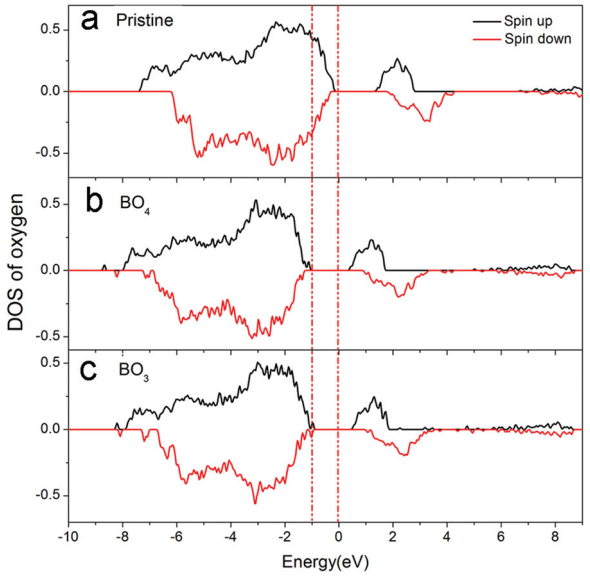

Figure 5. Calculated O DOS of B*x*-LRM. Calculated O DOS of a) $Li_{45}[Li_9Ni_6Co_6Mn2_4]O_{90}$, b) $Li_{45}[Li_9Ni_6Co_6Mn_{24}](BO_4)O_{86}$ with ^{IV}B in the site of "Li/Mn/Mn", and c) $Li_{45}[Li_9Ni_6Co_6Mn_{24}](BO_3)O_{87}$ with ^{III}B in the site of "Li/Co/Mn".

of O 1s electrons to the hybridized state of the metal 3d with O 2p orbitals.[24] The integral intensity of the pre-edge peak of the O K-edge spectra depends on the total d electronic holes in the states of metal 3d orbital hybridized with the O 2p orbital, or the covalency of the M-O bond.[25,26] It can be found that the integral intensity of the pre-edge peak of O decreases dramatically with respect to the *x* value. Combined with the metal L-edge results, this intensity change further confirms the decreased covalency of the M-O bonds. As indicated by many previous works, the strong covalency of active metals with oxygen, especially for Co-O, facilitates the generation of the electronic holes for the 2p band of oxygen and results in the evolution of oxygen under the high delithiated state.[27–30] Here, the decreased M-O covalence will alleviate the variation of the oxygen 2p band during cycling, which is one of the main reasons for the improved stability. Furthermore, as proposed by Goodenough in previous works, the polyanions $(X_mO_{3m+1})^{n-}$ will lower the top of the O 2p band effectively compared with that in layered oxides.[3] We demonstrate that, by incorporating boracic polyanions, the top of the O 2p band is lowered successfully by about 0.8 eV in $Li_{45}[Li_9Ni_6Co_6Mn_{24}]BO_{90}$ either with ^{IV}B or ^{III}B, as shown in **Figure 5**. Though the top of the O 2p band is still distinctly higher than for totally polyanion-type materials, such as $LiMPO_4$,[31] this will remarkably enhance the oxygen ion stability in this layered material under high voltage. The enhancement of the redox potential could be attributed to the strong polarization of oxygen atoms to boron, resulting in a decrease of the energies of antibonding d-electron redox couples of M due to the inductive effect,[32,33] and the stronger the polarization, the higher the potential.

To further reveal the origin of the enhanced stability, Ni, Co, and Mn K-edge ex-situ XANES of both B0-LRM and B0.02-LRM were collected. The samples after the 10th cycle were measured to avoid interference caused by the structure rearrangement during the initial cycles.[16] Since near edge signals of Ni involve a lot of Co extended edge signals, Ni K-edge EXAFS is not discussed here (detailed discussion of Ni K-edge XANES in Figure S8, Supporting Information). In **Figure 6**b, Co K-edge

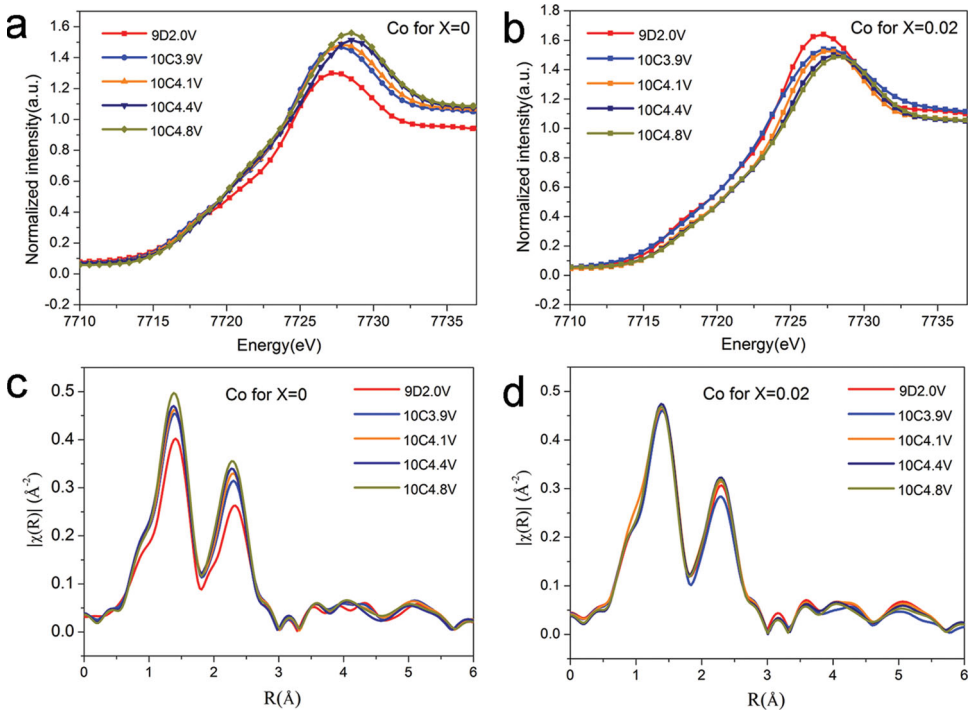

Figure 6. Ex-situ XAS of B*x*-LRM during the 10th charge process. Co K-edge XANES of a) B0-LRM and c) B0.02-LRM; b) and d) Fourier transformed EXAFS results obtained during the 10th charge process, respectively. "9D2.0V" refers to the spectra collected at 2.0 V in the 9th discharge process, the same applies to other curves.

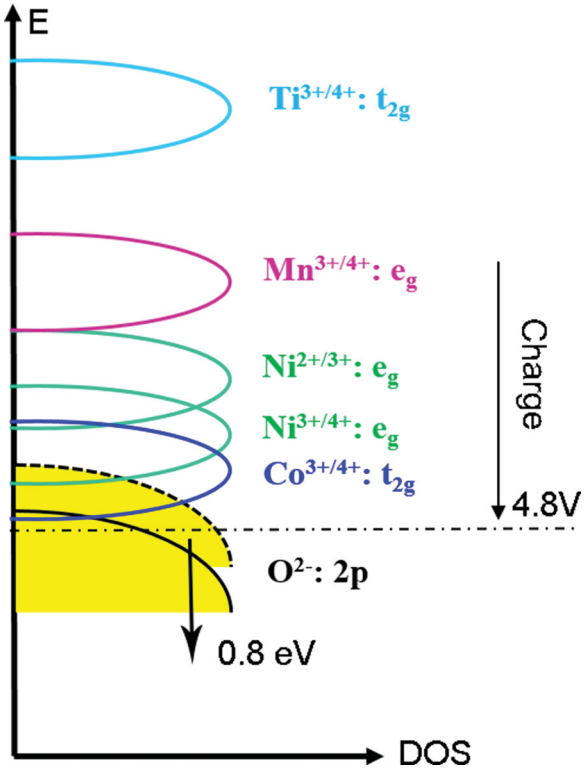

Figure 7. Schematic diagram of the charge compensation mechanism before and after the boracic polyanions substitution. The dashed line circled yellow area is the O 2p band before the substitution, while the solid circled area is the band after the substitution, lowered by about 0.8 eV.

spectra of B0.02-LRM show a larger shift of ≈1 eV than those of pristine B0-LRM (Figure 6a). Furthermore, the first peak in the radial structure functions of the Fourier transformed EXAFS spectrum of B0.02-LRM (Figure 6d) demonstrates less change under different delithiated states compared with that of B0-LRM (Figure 6c), implying a more stable Co-O octahedron environment. For B0-LRM, it is suggested that the large energy overlap of the Co^{4+}/Co^{3+} couple with the O 2p band results in weak changes for Co while most of the contribution of the charge compensation is realized by oxygen under the high delithiated state,[3,29,30] leading to oxygen evolution and structural collapse, similar to the case of $LiCoO_2$ and $LiNi_{1/3}Co_{1/3}Mn_{1/3}O_2$.[24,25] However, after the incorporation of boracic polyanions, Co will take large valence changes to compensate for the charge, and little holes will be generated on the O 2p band, as shown in **Figure 7**. The Mn K-edge ex-situ XAS in Figure S9 (Supporting Information) further demonstrated that less structural variation of Mn-O coordination is present in B0.02-LRM. Thus, the stability of the MO_6 environment and the layered structure is improved.

3. Conclusion

In summary, we successfully demonstrated a new strategy to improve the performance of layered cathodes by manipulating the electronic structure through incorporation of the polyanions $(BO_3)^{3-}$ and $(BO_4)^{5-}$. The materials showed a strongly improved specific capacity, cycling performance, enhanced redox potentials, and superior thermal stability. We attribute this improved performance to the decreased covalency of the M-O bonds and the lowered top of the O 2p band, which may alleviate the variation of the electronic structure of the O 2p band induced during the delithiation and lithiation process. We note that this novel combination of polyanions with layered materials was proposed and realized for the first time. Furthermore, polyanions like $(PO_4)^{3-}$, $(SO_4)^{2-}$, and $(SiO_4)^{4-}$ may have the same potential to realize this improvement, and the strong covalency of P-O, S-O, and Si-O may have the same effect to tune the electronic structure of the M-O systems, which will be extended to other work regarding cathode preparation.

4. Experimental Section

Sample Preparation: $Li_{1.2}Ni_{0.13}Co_{0.13}Mn_{0.54}(BO_4)_{0.75x}(BO_3)_{0.25x}O_{2-3.75x}$ was synthesized via a sol-gel method to obtain the precursor. Stoichiometric amounts of lithium acetate dihydrate (5% excess), nickel acetate tetrahydrate, manganous acetate tetrahydrate, cobaltous acetate tetrahydrate, and boracic acid were mixed together and dissolved in deionized water with citric acid as the complexant and ethylene glycol as the dispersant. The sol was evaporated using a rotary evaporator leading to the formation of a hydrous gel. The hydrous gel was then dried at 150 °C for 8 h. After the dried gel was milled with a mortar and a pestle, it was sintered at 450 °C for 4 h and then at 850 °C for 15 h to get the target products.

Structure Analysis: To investigate the crystal structure of the layered materials before and after the substitution, X-ray diffraction (XRD) was measured using a D8-Advance diffractometer (Bruker, Germany) with Cu Kα radiation (λ = 1.5406 Å) operated at 40 kV and 40 mA. The scan data were collected in a 2θ range of 10–80°, with a step size of 0.02° and a counting time of 4 s. Intermediate infrared spectra (4000 cm^{-1}–400 cm^{-1}) were recorded using a Fourier transform infrared (FTIR) spectrometer (Bruker VECTOR22) equipped with MCT mid-IR, ATR and so on. The powder was mixed with KBr to make a transparent slice for IR radiation and the data were collected in absorption mode. The morphological characteristics of the powders were evaluated using cold field emission scanning electron microscopy (SEM, Hitachi S-4800) and transmission electron microscopy (TEM, FEI, TECNAI F20).

Electrochemical Testing and DSC Measurements: The cathode electrode was prepared by pasting a mixture of 80 wt% active material, 10 wt% Super P, and 10 wt% polyvinylidene fluoride (PVDF) on an aluminum foil. Before fabrication, the cathode electrode was dried at 120 °C overnight. The electrolyte was purchased from the Beijing Institute of Chemical Reagents and the ingredient is confidential, and Whatman glass microfiber filters were used as the separator. The R2032-type coin cells were taken for electrochemical testing and fabricated with Li metal as the anode in the argon filled glovebox, in which the oxygen and moisture content was below 0.5 ppm. The galvanostatic charge/discharge process for all of the materials was measured by a NEWARE tester at room temperature (25 °C), except for the high temperature (65 °C) tests. DSC measurements were performed to monitor the thermostability of these materials using a Mettler (DSC–1) instrument at a rate of 10 °C min^{-1} to 400 °C. Samples were prepared by charging the cells at 4.6 V at the second cycle and maintained at a constant voltage for 10 h, and then disassembled in an argon-filled glove box. The cathode material was sealed in an aluminum DSC pan with an additional 1 µL new electrolyte before taken out from glove box for the measurement.

X-ray Absorption Spectroscopy: Hard XAS of Mn, Ni, Co K-edge spectra were collected in fluorescence mode at beamline 1W2B with a Si (111) double-crystal monochromator in the Beijing Synchrotron Radiation Facility (BSRF). To prepare the samples during the charge process for ex-situ measurements, all of the cells were charged and discharged at a current density of 60 mA g^{-1}, and then disassembled in the argon-filled glove box. The materials coated on an Al foil were sealed by 3M tape

before taken out and packed in a bag full of argon. Energy calibration was carried out by the first inflection point of the Mn, Ni and Co foil as the reference (Mn K-edge = 6539 eV, Co K-edge = 7709 eV and Ni K-edge = 8333 eV). The XAS data analysis was carried out using standard procedures by IFEFFIT. The spectrum below the pre-edge region was fitted to a straight line, and the postedge background was subtracted based on the cubic spline procedure. The normalized EXAFS spectra were converted from E space to k space weighted by k, and then converted to R space. Soft XAS data of the Mn, Ni, Co L-edge and O, B K-edge were collected in the total electron yield (TEY) mode at beamline 4B7B in the Beijing Synchrotron Radiation Facility (BSRF). The energy calibration was performed using the H_3BO_3 standard sample. The peak-differentiating analysis of B K-edge XAS was performed by the software XPSPEAK41, with the value of sum of χ^2 below 1. The data were analyzed first by background subtraction using the Shirley routine and a subsequent nonlinear fitting by mixed Gaussian–Lorentzian functions.

Computational Methods: All the first principles calculations were performed with the VASP (Vienna ab inito simulation package) within the projector augmented-wave (PAW) approach.[34–36] The data were obtained within the GGA+U scheme. The Hubbard U value for Ni-3d, Co-3d and Mn-3d was 6.30, 4.91, and 4.95 eV, respectively, according to previous theoretical work.[37,38] The spin polarization of the ferromagnetic configuration was considered. The Monkhorst-Pack scheme 2×1×1 k-points mesh was used for the integration in the irreducible Brillouin zone. The Energy cutoff for the plane waves was chosen to be 520 eV. The lattice parameters and the ionic position of the structure were fully relaxed, and the final forces on every relaxed atoms were less than 0.05 eV $Å^{-1}$.

Supporting Information

Supporting Information is available from the Wiley Online Library or from the author.

Acknowledgements

D.X. designed the experiments. B.L. and J.M. performed the experiments and data analysis. H.J., P.Y., W.H., W.C., and Z.W. conducted the calculations. D.X. guided the whole work and analysis. B.L., D.X., and Z.W. wrote the paper. This work was supported by the National Basic Research Program of China (2013CB934004), the Ministry of Science & Technology of China (2012CB825800), the National Natural Science Foundation of China (11179001), the Science Fund for Creative Research Groups (11321503) of NSFC, the National High Technology Research and Development Program (No.2012AA052201), and the major program of the Beijing Municipal Natural Science Foundation (20110001). The help in measuring the XAS spectra from Beijing Synchrotron Radiation Facility (BSRF) is highly appreciated.

Received: February 8, 2014
Revised: March 12, 2014
Published online: June 6, 2014

[1] K. Kang, Y. S. Meng, J. Bréger, C. P. Grey, G. Ceder, *Science* **2006**, *311*, 977.
[2] Y.-K. Sun, S.-T. Myung, B.-C. Park, J. Prakash, I. Belharouak, K. Amine, *Nat. Mater.* **2009**, *8*, 320.
[3] J. B. Goodenough, K.-S. Park, *J. Am. Chem. Soc.* **2013**, *135*, 1167.
[4] S.-K. Jung, H. Gwon, J. Hong, K.-Y. Park, D.-H. Seo, H. Kim, J. Hyun, W. Yang, K. Kang, *Adv. Energy Mater.* **2014**, *4*, 1300787.
[5] H. Lee, Y. Kim, Y.-S. Hong, Y. Kim, M. G. Kim, N.-S. Shin, J. Cho, *J. Electrochem. Soc.* **2006**, *153*, A781.
[6] N. Yabuuchi, K. Yoshii, S. T. Myung, I. Nakai, S. Komaba, *J. Am. Chem. Soc.* **2011**, *133*, 4404.
[7] Z. Wang, B. Li, J. Ma, D. Xia, *Electrochim. Acta* **2014**, *117*, 285.
[8] M. Gu, I. Belharouak, J. Zheng, H. Wu, J. Xiao, A. Genc, K. Amine, S. Thevuthasan, D. R. Baer, J.-G. Zhang, N. D. Browning, J. Liu, C. Wang, *ACS Nano* **2013**, *7*, 760.
[9] J. Zheng, M. Gu, J. Xiao, P. Zuo, C. Wang, J.-G. Zhang, *Nano. Lett.* **2013**, *13*, 3857.
[10] Z. Li, N. A. Chernova, J. J. Feng, S. Upreti, F. Omenya, M. S. Whittingham, *J. Electrochem. Soc.* **2012**, *159*, A116.
[11] Y.-K. Sun, M.-J. Lee, C. S. Yoon, J. Hassoun, K. Amine, B. Scrosati, *Adv. Mater.* **2012**, *24*, 1192.
[12] F. Wu, N. Li, Y. Su, H. Shou, L. Bao, W. Yang, L. Zhang, R. An, S. Chen, *Adv. Mater.* **2013**, *25*, 3722.
[13] J. Liu, M. Hou, J. Yi, S. Guo, C. Wang, Y. Xia, *Energy Environ. Sci.* **2014**, *7*, 705.
[14] X. Zhang, I. Belharouak, L. Li, Y. Lei, J. W. Elam, A. Nie, X. Chen, R. S. Yassar, R. L. Axelbaum, *Adv. Energy Mater.* **2013**, *3*, 1299.
[15] Z. Gong, Y. Yang, *Energy Environ. Sci.* **2011**, *4*, 3223.
[16] A. R. Armstrong, M. Holzapfel, P. Novak, C. S. Johnson, S. H. Kang, M. M. Thackeray, P. G. Bruce, *J. Am. Chem. Soc.* **2006**, *128*, 8694.
[17] D. Li, G. M. Bancroft, M. E. Fleet, *J. Electron Spectrosc. Relat. Phenom.* **1996**, *79*, 71.
[18] M. E. Fleet, S. Muthupari, *J. Non-Cryst. Solids* **1999**, *255*, 233.
[19] M. E. Fleet, S. Muthupari, *Am. Mineral.* **2000**, *85*, 1009.
[20] K. Simmance, G. Sankar, R. G. Bell, C. Prestipino, W. v. Beek, *Phys. Chem. Chem. Phys.* **2010**, *12*, 559.
[21] T. Yamamoto, *X-Ray Spectrom.* **2008**, *37*, 572.
[22] Z. Y. Wu, D. C. Xian, T. D. Hu, Y. N. Xie, Y. Tao, C. R. Natoli, E. Paris, A. Marcelli, *Phys. Rev. B* **2004**, *70*, 033104.
[23] J. Liu, H. Chen, J. Xie, Z. Sun, N. Wu, B. Wu, *J. Power Sources* **2014**, *251*, 208.
[24] W.-S. Yoon, M. Balasubramanian, K. Y. Chung, X.-Q. Yang, J. McBreen, C. P. Grey, D. A. Fischer, *J. Am. Chem. Soc.* **2005**, *127*, 17479.
[25] W.-S. Yoon, K.-B. Kim, M.-G. Kim, M.-K. Lee, H.-J. Shin, J.-M. Lee, J.-S. Lee, C.-H. Yo, *J. Phys. Chem. B* **2002**, *106*, 2526.
[26] W.-S. Yoon, M. Balasubramanian, X.-Q. Yang, Z. Fu, D. A. Fischer, J. McBreen, *J. Electrochem. Soc.* **2004**, *151*, A246.
[27] P. Xiao, Z. Q. Deng, A. Manthiram, G. Henkelman, *J. Phys. Chem. C* **2012**, *116*, 23201.
[28] Z. Q. Deng, A. Manthiram, *J. Phys. Chem. C* **2011**, *115*, 7097.
[29] A. Ito, Y. Sato, T. Sanada, M. Hatano, H. Horie, Y. Ohsawa, *J. Power Sources* **2011**, *196*, 6828.
[30] M. Oishi, T. Fujimoto, Y. Takanashi, Y. Orikasa, A. Kawamura, T. Ina, H. Yamashige, D. Takamatsu, K. Sato, H. Murayama, H. Tanida, H. Arai, H. Ishii, C. Yogi, I. Watanabe, T. Ohta, A. Mineshige, Y. Uchimoto, Z. Ogumi, *J. Power Sources* **2013**, *222*, 45.
[31] L. Wang, L. Zhang, J. Li, J. Gao, C. Jiang, X. He, *Int. J. Electrochem. Sci.* **2012**, *7*, 3362.
[32] A. K. Padhi, K. S. Nanjundaswamy, C. Masquelier, S. Okada, J. B. Goodenough, *J. Electrochem. Soc.* **1997**, *144*, 1609.
[33] A. K. Padhi, K. S. Nanjundaswamy, J. B. Goodenough, *J. Electrochem. Soc.* **1997**, *144*, 1188.
[34] G. Kresse, J. Hafner, *Phys. Rev. B* **1993**, *47*, 558.
[35] G. Kresse, J. Furthmüller, *Comput. Mater. Sci.* **1996**, *6*, 15.
[36] G. Kresse, D. Joubert, *Phys. Rev. B* **1999**, *59*, 1758.
[37] G. Trimarchi, N. Binggeli, *Phys. Rev. B* **2005**, *71*, 035101.
[38] F. Zhou, M. Cococcioni, C. A. Marianetti, D. Morgan, G. Ceder, *Phys. Rev. B* **2004**, *70*, 235121.